

Wind Turbine Project

Part I: Wave Dynamics at Bretagne Sud

Louis Yue Ting Shing, *M2 STEEM, Ecole Polytechnique*

I. INTRODUCTION

A. Context and motivation

Offshore wind design depends on local metocean conditions because waves control platform motions, mooring loads, marine access, and fatigue. For floating wind turbines, hydrodynamic excitation couples to pitch, surge, and heave, so both the typical operating environment and the rare storms must be characterised with care. A long hindcast record paired with targeted comparison to a nearby buoy provides the basis for this characterisation at the selected study area in Bretagne Sud 1 [1], [2], [3]. The analysis in this report focuses on significant wave height, mean period, peak period, and approach direction, with attention to seasonal variability and the implications for subsequent numerical modelling and load assessment.

B. Statement of purpose

The purpose is to quantify the mean and seasonal wave climate at the study site using a multi-decadal hindcast, to assess the representativeness of that hindcast through comparison with a nearby wave buoy, and to estimate extreme conditions at one-year and fifty-year return periods via standard extreme value analysis (EVA). Block-maxima (BM) and peaks-over-threshold (POT) methods are applied to derive return levels for significant wave height, and associated peak period and approach direction are inferred to support floating wind design. To relate univariate extremes to realistic storm pairings, a multivariate environmental contour in height and period is constructed using a principal-component inverse first-order reliability method (I-FORM) approach, providing admissible design combinations for subsequent load cases.

C. Report outline

The report defines the study site, dataset, and conventions; describes long-term means, common sea states, and seasonal variability; evaluates hindcast skill against a nearby buoy; estimates one- and fifty-year extremes using BM and POT with diagnostics; and constructs a height-period environmental contour to supply design pairings. The closing section summarises implications for floating wind applications and points to priorities for refinement.

II. STUDY SITE, DATA, AND CONVENTIONS

The analysis point lies within the Bretagne Sud 1 implantation zone. The purpose of this section is to fix the geographic target, describe the hindcast dataset on which the study relies, and state the processing and directional conventions applied throughout.

The target location was defined from the official project polygon and mapped to the nearest node of the unstructured computational mesh. The selected node (ID 117231) is 1.409 km from (47.3236°N, −3.5522°E) in WGS-84. This offset is small relative to the offshore mesh scale and is adequate for characterising the local offshore wave climate. Figure 1 situates the analysis point west of Quiberon and Belle-Île-en-Mer and confirms that it lies well offshore of coastal complexity.

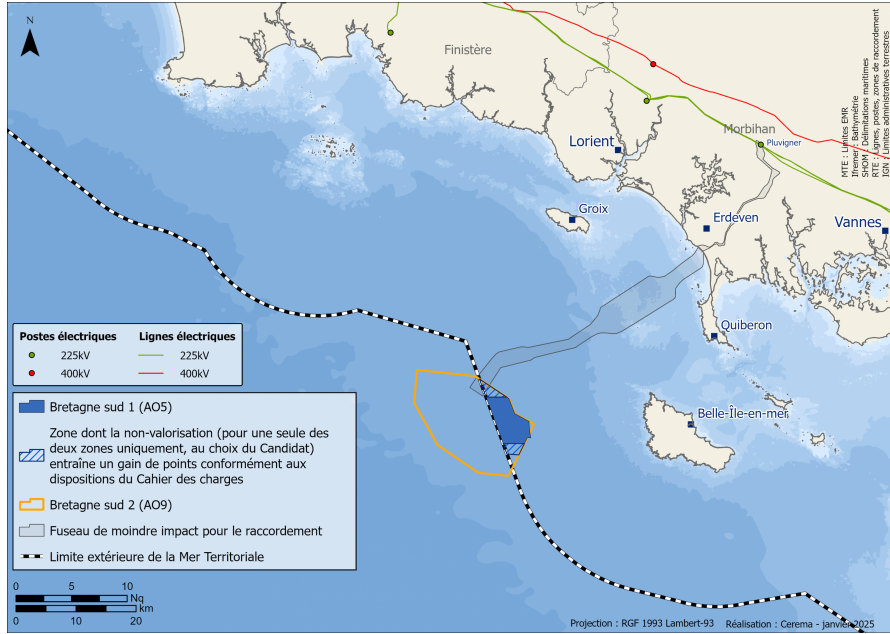


Figure 1: Bretagne Sud 1 implantation zone with the analysis point marked. The map provides geographic context and confirms the offshore position used for hindcast extraction [3].

Wave, wind, and surface-current time series were extracted from the RESOURCECODE hindcast. The database provides WAVEWATCH III (v7.08) spectral simulations on an unstructured mesh for 1994–2020, forced by ERA5 winds and barotropic tidal currents [1]. Hourly outputs from 1994-01-01 00:00 UTC to 2020-12-31 23:00 UTC were obtained at node 117231 and form the basis for all subsequent analyses.

Local mesh sampling and bathymetry are shown in figure 2. The node density increases near the shore and islands and is quasi-regular offshore, and the chosen node sits in a well-resolved region. The bathymetry indicates a gently sloping shelf that deepens to the southwest. At the analysis point the mean water depth is 93.32 m with a standard deviation of 1.18 m across the record, which indicates weak tidal level modulation for the integral parameters considered here.

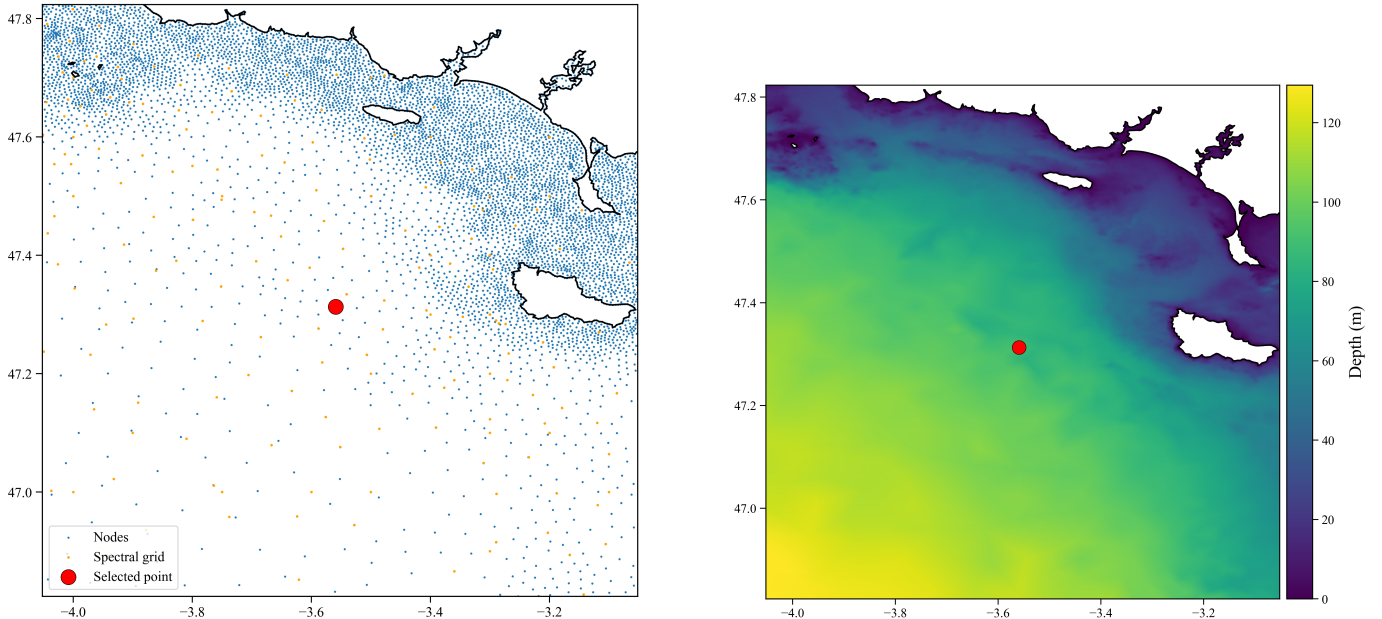


Figure 2: Location and local context of the RESOURCECODE analysis point. Left: position within the unstructured grid; the selected node (red, ID 117231) lies near 47.32° N, 3.55° W. Right: corresponding bathymetry referenced to mean sea level with the selected node marked. The selected node is ~ 1.4 km from the target coordinates.

The study uses the following fields and derived quantities, reported at the native hourly resolution. Directions are expressed clockwise from geographic North. Waves and winds are treated as coming-from; surface currents are treated as going-to.

Table I: Core metocean parameters and units used in the analysis.

Quantity	Definition or meaning	Units
Significant wave height H_{m0}	$4\sqrt{m_0}$ from the variance spectrum	m
Mean zero-crossing period T_{m02}	$2\pi\sqrt{m_0/m_2}$	s
Mean wave direction	Spectral mean, coming-from	°
Directional spreading	Spectral spread parameter	°
Peak frequency f_p	Frequency at spectral maximum	Hz
Peak period T_p	$1/f_p$	s
Wind speed U_{10}	Magnitude from east–north components	m s^{-1}
Wind direction	Coming-from	°
Surface current speed	Magnitude from east–north components	m s^{-1}
Surface current direction	Going-to	°
Water depth h	Bathymetric depth at node	m

Timestamps are handled in UTC. All quantities are expressed in SI units, and reported magnitudes are rounded consistently with the dataset precision. External consistency is discussed later through a comparison with the Candhis Belle-Île buoy under matched timestamps and common directional conventions [2].

In summary, node 117231 provides an appropriate offshore analysis point for Bretagne Sud 1: it lies within the implantation zone, is well resolved by the mesh, sits in approximately 93 m of water, and offers a complete hourly record with explicit and consistent conventions for waves, winds, and currents.

III. MEAN WAVE CONDITIONS AND SEASONAL VARIABILITY

A. Mean Wave Conditions and Trend Analysis (1994–2020)

The purpose of this subsection is to quantify long-term mean wave conditions at the Bretagne Sud site and to assess whether secular trends exist over 1994–2020. The practical relevance is to evaluate whether mean conditions are likely to change appreciably within a 30 year offshore wind turbine lifetime.

1) *Methodology:* Hourly hindcast series were aggregated to monthly means for significant wave height H_{m0} and mean zero-crossing period T_{m02} to reduce short-term noise while retaining seasonal variability. The wave direction was treated using monthly circular means of the coming-from convention to respect the angular nature of the variable and avoid averaging artefacts near the $0^\circ/360^\circ$ discontinuity.

Linear trends were estimated on the monthly series with ordinary least squares (OLS) against time in years. For direction, the monthly circular-mean series was first unwrapped in radians before regression and then re-wrapped for presentation, ensuring a physically consistent estimate of directional drift in degrees per decade.

A non-parametric Mann–Kendall (MK) test with Sen’s slope was applied to each monthly series to test for monotonic trends that may not be well represented by a linear model. Statistical significance was evaluated at $\alpha = 0.05$ with $n = 324$ monthly values for each variable [4].

2) *Results and Interpretations:* The information sought was whether monthly means of H_{m0} , T_{m02} , and coming-from direction display sustained multi-decadal changes and, if present, their magnitudes. A regression of monthly means against time was performed, and a monotonic trend test was applied. Then estimates and uncertainty from OLS and MK approaches were compared.

Figure 3 presents the monthly series of H_{m0} , T_{m02} , and coming-from direction for 1994–2020 together with OLS fits.

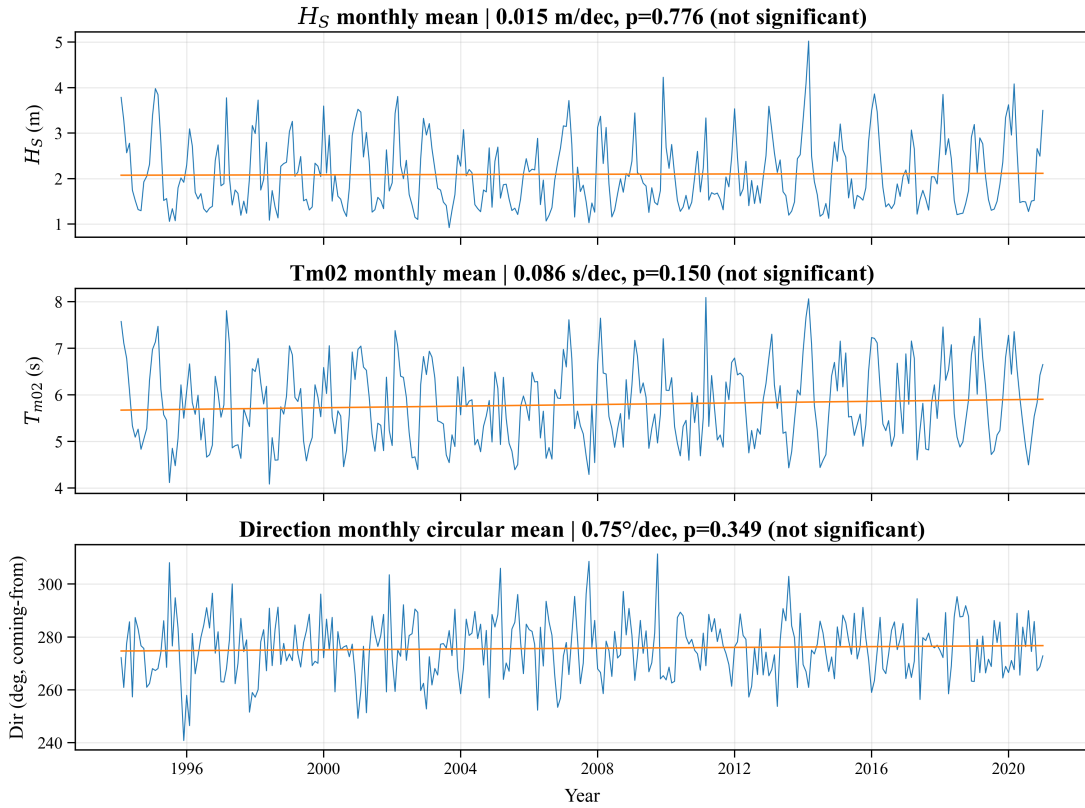


Figure 3: Monthly mean wave conditions show strong seasonality but no secular trend at Bretagne Sud, 1994–2020. Time series of monthly means for significant wave height H_{m0} (top), mean zero-crossing period T_{m02} (middle), and coming-from direction (bottom); blue curves are monthly means and orange lines are OLS fits. Panel titles report OLS slopes per decade and p -values.

The figure shows pronounced seasonality and marked interannual variability in H_{m0} and T_{m02} , with the highest values during boreal winter and lower values during summer. The coming-from direction fluctuates mostly within 260° – 290° with episodic deviations but without a visually coherent multi-decadal drift.

Taken together, the short mean period $\overline{T_{m02}} = 5.785$ s and moderate mean height $\overline{H_{m0}} = 2.092$ m indicate a locally forced wind sea; a swell-dominated mean in the North-East Atlantic would yield $T_{m02} \gtrsim 10$ s. The mean coming-from direction of 275.5° follows the Bay of Biscay fetch geometry: open ocean to the west and land to the east and south constrain opposing sectors, so the climatological incidence is westerly. At $h = 93.32$ m most, sea states are deep water for these periods, limiting shoaling and refraction offshore and reinforcing a wind-sea-dominated Atlantic exposure with winter intensification.

Quantitative trend estimates from OLS and MK are reported in Table II, which also lists the implied 30 year changes from the OLS slopes. The OLS slopes are small in magnitude for all variables and are associated with p -values greater than 0.05, while MK p -values also exceed 0.05 and Sen's slopes closely match the OLS magnitudes.

Table II: Monthly mean wave climate at Bretagne Sud shows no statistically significant trends (1994–2020). Trends were estimated from monthly means by OLS and by the MK test with Sen's slope. Wave directions use coming-from circular means unwrapped for linear modelling. Sample size, $n = 324$ months and $\alpha = 0.05$. Slopes are per decade; Δ_{30y} is derived from the OLS slope. Reported p -values correspond to each method, and the “Verdict” column indicates whether $p < 0.05$.

Variable	OLS slope	OLS p	n	Δ_{30y}	MK Sen slope	MK p	Verdict
H_{m0} (m)	+0.015 m/dec	0.776	324	+0.046 m	+0.012 m/dec	0.810	not significant
T_{m02} (s)	+0.086 s/dec	0.150	324	+0.259 s	+0.084 s/dec	0.196	not significant
Direction (°)	+0.750°/dec	0.349	324	+2.26°	+0.660°/dec	0.441	not significant

The absence of statistical significance in both OLS and MK indicates no detectable secular trends in mean H_{m0} , mean T_{m02} , or mean coming-from direction over 1994–2020 within the hindcast record. The OLS-implied 30 year changes are ≈ 0.05 m for H_{m0} , ≈ 0.26 s for T_{m02} , and $\approx 2.3^\circ$ for direction, which are small relative to the seasonal cycle and interannual variability seen in figure 3.

It is therefore expected that mean wave conditions will not change appreciably over a 30 year turbine lifetime if future variability resembles the 1994–2020 hindcast. This inference is conditional on the stationarity of the forcing and the modelling system; climate-driven shifts not resolved within the period or by the hindcast could alter the mean state, but such effects are not identifiable from the present analysis.

B. Most Common Wave Conditions

The aim of this subsection was to identify the most frequent operating sea states and to determine whether waves at the site behave as deep, transitional, or shallow water waves. This informs the validity of deep-water kinematics for load modelling.

1) Methodology: Hourly hindcast records were quality-controlled to retain finite values of H_{m0} , T_{m02} , coming-from direction, and local depth. A two-dimensional histogram of (T_{m02}, H_{m0}) was constructed to estimate the empirical joint density. The modal bin is defined as the single (T_{m02}, H_{m0}) bin with the highest probability density; it represents the most typical sea state in the record, rather than an arithmetic mean.

To improve readability and avoid density flattening by extreme values, plot axes were limited to the central 99 % of each variable by trimming to the 0.5th–99.5th percentiles of H_{m0} and T_{m02} . This trimming removes a small set of outliers ($\lesssim 0.5\%$ of hours) from the plotting window without affecting the physical interpretation of the wave climate; consequently, a few very long-period events that fall in the transition range do not appear in the panel.

Deep-water and linear shallow-water thresholds were evaluated at the mean depth $h = 93.32$ m (standard deviation 1.20 m). Using the period form $T\sqrt{g/h}$, the limits are $T_{\text{deep}} = 4\sqrt{h/g} = 12.34$ s and $T_{\text{linear}} = 25\sqrt{h/g} = 77.11$ s. Shares of occurrences in each regime were computed from T_{m02} using this period criterion and, independently, using a fast wavelength screen $L_{\text{approx}} = gT^2/(2\pi)$ with the classical h/L limits. Only non-zero, finite data points were counted [5].

2) Results and Interpretations: The information sought was the location of the most common sea state in (T_{m02}, H_{m0}) space and whether typical conditions fall within the deep-water regime. Hence, a joint-density histogram annotated with the deep- and linear-threshold periods and with the modal bin marked was plotted and can be seen in figure 4.

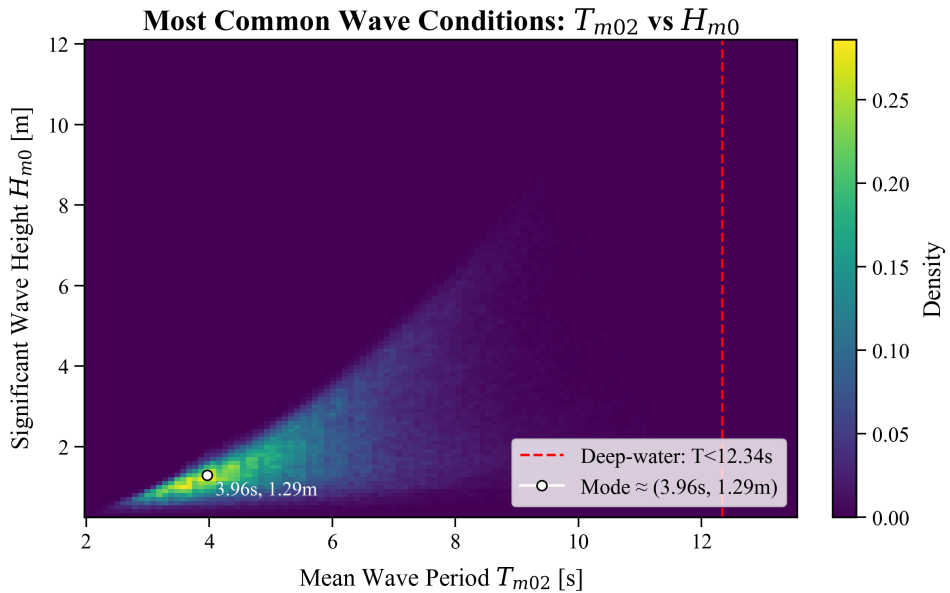


Figure 4: Bretagne Sud sea states are overwhelmingly deep-water; the modal condition is short-period and low-height. Shown is a 2D histogram of hourly hindcast data (1994–2020) of T_{m02} versus H_{m0} ; axes are trimmed to the 0.5th–99.5th percentiles to emphasise the dominant climate. The shallow-water limit $T_{\text{linear}} = 25\sqrt{h/g} = 77.11$ s lies beyond the plotted range.

The figure shows a compact high-density core centred on short-to-moderate periods and low-to-moderate heights, with a sparse tail towards larger T_{m02} and H_{m0} . The modal bin lies at $T_{m02} \approx 3.59$ s and $H_{m0} \approx 1.00$ m, indicating that the most typical sea state is a low sea with short period. The deep-water threshold at 12.34 s lies to the right of almost all observations in the plotting window.

It is observed that the site operates almost entirely in deep water. Using the period criterion, the deep-water share is 99.98 %, the transitional share is 0.02 %, and no shallow-water cases are detected. Using the wavelength screen, the corresponding shares

are 99.76 % deep, 0.24 % transitional, and 0.00 % shallow. The small difference between diagnostics reflects the conservatism of the exact period test relative to the L_{approx} screen. The low depth variability (standard deviation 1.20 m) supports the use of the mean depth for regime classification. For subsequent hydrodynamic calculations, deep-water dispersion is therefore appropriate for nearly all sea states.

The information sought next was the prevailing wave incidence sector and its relationship with sea-state energy. Hence, figure 5 was produced, showing a coming-from wave rose binned by direction and stacked by H_{m0} classes to apportion total occurrence by both sector and height.

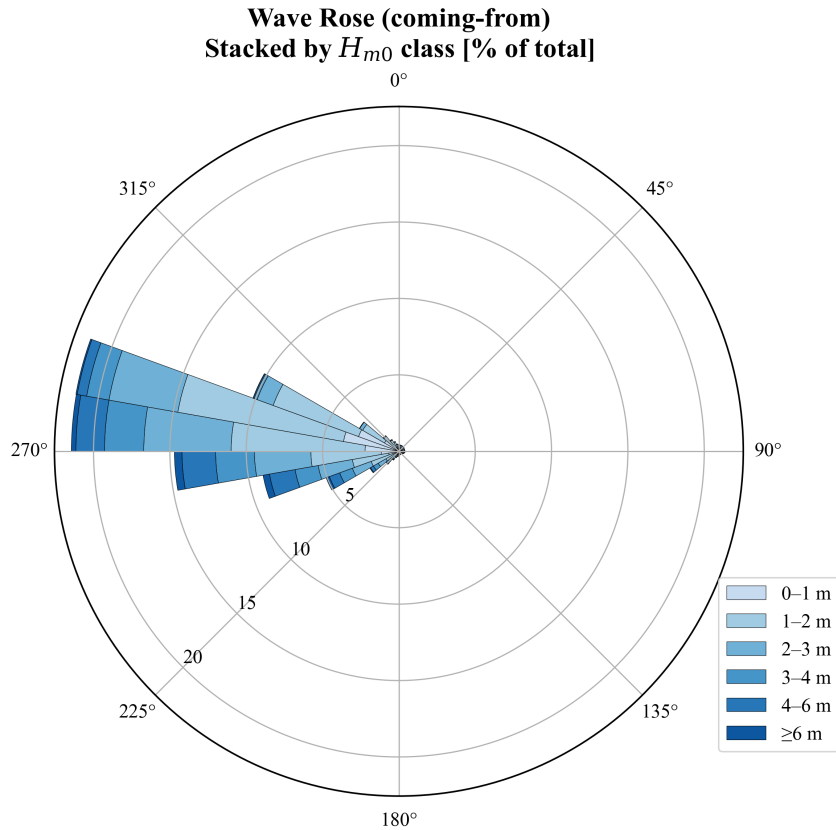


Figure 5: Waves at Bretagne Sud arrive predominantly from the west; most hours have low–moderate height and rare high waves originate from the same sector. Shown is a coming-from wave rose of hourly hindcast records (1994–2020); angles are clockwise from true North with 0° at the top. Bars give the percentage of all valid hours per directional sector and are stacked by H_{m0} class.

The figure shows a dominant westerly sector centred near 270°, with smaller contributions from adjacent west-south-west and west-north-west sectors. Most occurrences belong to $H_{m0} < 3$ m classes, while higher-wave events are infrequent but aligned with the same westerly sector.

This is consistent with exposure to the North Atlantic, which generates a stable westerly incidence at the site. The directional concentration supports the use of sector-specific design checks aligned about 270°, while the deep-water dominance justifies linear deep-water kinematics for load estimation.

In conclusion, the site's most typical sea state is $T_{m02} \approx 3.59$ s and $H_{m0} \approx 1.00$ m, and more than 99.7 % of hours satisfy deep-water criteria. Waves arrive predominantly from the west. These characteristics simplify subsequent modelling by allowing deep-water assumptions and a narrow directional focus.

C. Seasonal variability

The objective was to test whether the mean sea state follows a seasonal cycle in height, period, and approach direction, and to quantify its timing and amplitude so that operability windows and the subsequent extremes analysis are placed in an appropriate climatological context.

1) Methodology: The goal was to obtain a month-by-month characterisation of the central tendency and typical spread of H_s , T_{m02} , and the mean coming-from direction, together with any systematic seasonal phasing among these variables. Hourly hindcast values at the study node (1994–2020) were aggregated by calendar month.

For H_s and T_{m02} , arithmetic monthly means and interquartile ranges (IQRs, 75th–25th percentiles) were computed. For direction, circular monthly means and circular standard deviations were computed under the coming-from, clockwise-from-true-North convention; monthly means were unwrapped around the overall circular mean ($\approx 275.5^\circ$) to avoid the $0^\circ/360^\circ$ discontinuity. Sample sizes per month were $n = 20\,088$ h for 31-day months, $n = 19\,440$ h for 30-day months, and $n = 18\,312$ h for February; all months were retained after quality control (QC).

2) Results and Interpretations: The resulting monthly climatology is displayed in figure 6.

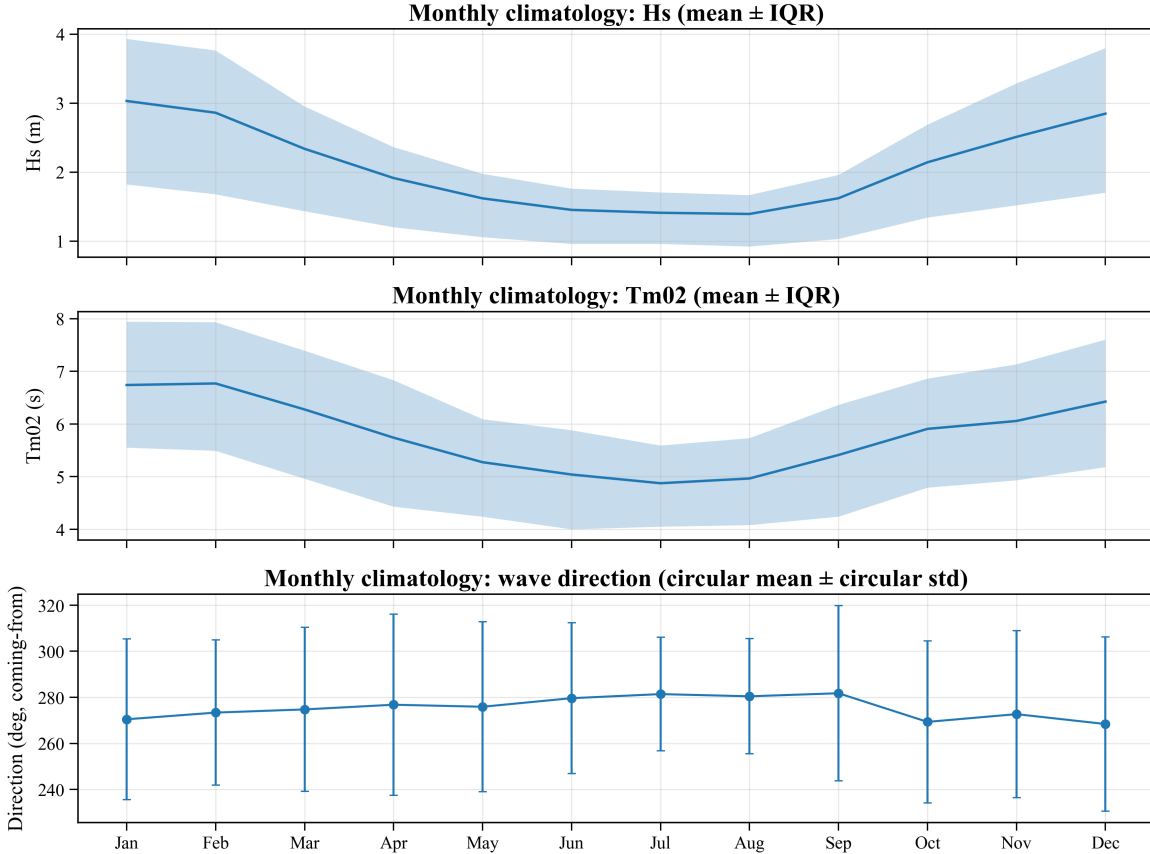


Figure 6: Winter seas are higher, longer, and approach from due west, while summer seas are lower and veer slightly toward WNW. Monthly statistics are computed from hourly RESOURCECODE hindcast at the study node over 1994–2020: H_s and T_{m02} are shown as mean \pm IQR, and direction as circular mean \pm circular standard deviation under the coming-from, clockwise-from-true-North convention. Replicates per month are $n = 20,088$ h for 31-day months, $n = 19,440$ h for 30-day months, and $n = 18,312$ h for February; no months were excluded after QC.

A clear annual cycle is evident in both H_s and T_{m02} . Heights are largest in winter and smallest in summer, with an observed peak in January and a trough in August for H_s ; periods peak in February and are shortest in July for T_{m02} . Winter means exceed $H_s > 2.5$ m and $T_{m02} \approx 6.8$ s, whereas summer means are about $H_s \approx 1.5$ m and $T_{m02} \approx 5.0$ s. The IQR widens in winter and narrows in summer, indicating broader condition ranges during the storm season.

The approach direction exhibits a modest seasonal veer. Winter means cluster near due west ($\approx 270^\circ$), while summer means shift slightly toward west-north-west (about 280°). The circular standard deviation is of comparable magnitude across months, with only a shallow minimum during mid-summer, indicating limited seasonal change in directional spread.

These patterns are consistent with seasonal atmospheric forcing over the North Atlantic. During boreal winter the storm track intensifies and fetch increases, producing larger and longer-period seas that propagate into the Bay of Biscay; during summer a strengthened Azores High favours weaker winds and shorter effective fetch, yielding lower heights and shorter periods. The

small directional veer aligns with the transition from more zonal winter flow to slightly more north-westerly summer swell incidence.

In conclusion, the site displays a robust annual cycle with higher, longer, and more variable seas in winter, a slight summer veer toward WNW, and near-constant directional spread. These results support preferential scheduling of weather-sensitive operations from late spring to summer and provide the seasonal context for conditioning the extremes analysis.

D. Mean Wind and Current Conditions

The objective was to characterise the typical wind and current regime at the study site and to determine whether a seasonal cycle is present in magnitude and direction.

1) Methodology: Wind and current time series from RESOURCECODE for 1994–2020 were analysed, with direction treated on a circular scale. Eastward and northward components (u, v) were converted to headings measured clockwise from true North with $0^\circ = N$. The going-to bearing was computed as $\theta_{\text{to}} = \text{mod}(\text{atan}2(u, v) \cdot 180/\pi, 360)$, and the coming-from bearing used for winds as $\theta_{\text{from}} = \text{mod}(\theta_{\text{to}} + 180, 360)$. Circular means were obtained from unit vectors as $\bar{\theta} = \arg(\sum_i e^{i\theta_i})$, and arithmetic means were used for speeds.

Calms were excluded for rose construction only, using thresholds of 0.5 m/s for wind and 0.05 m/s for currents to avoid spurious dominance of the calm sector. Occurrence roses were produced for the full period and by season (DJF, MAM, JJA, SON) to visualise directional frequency jointly with speed classes. The wind roses used 22.5° sectors and speed bins $[0.5, 2], [2, 4], \dots, \geq 16$ m/s; the current roses used 10° sectors and speed bins $[0.05, 0.10], [0.10, 0.15], [0.15, 0.20], \geq 0.20$ m/s. Because the currents reverse tidally along a principal axis, an overall circular-mean current direction is not physically representative.

2) Results and Interpretations: The information sought was the prevailing wind approach and how it varies seasonally. Consequently, occurrence roses for all data and for each season under the coming-from convention were computed, with calms excluded. The relevant results are presented in figure 7.

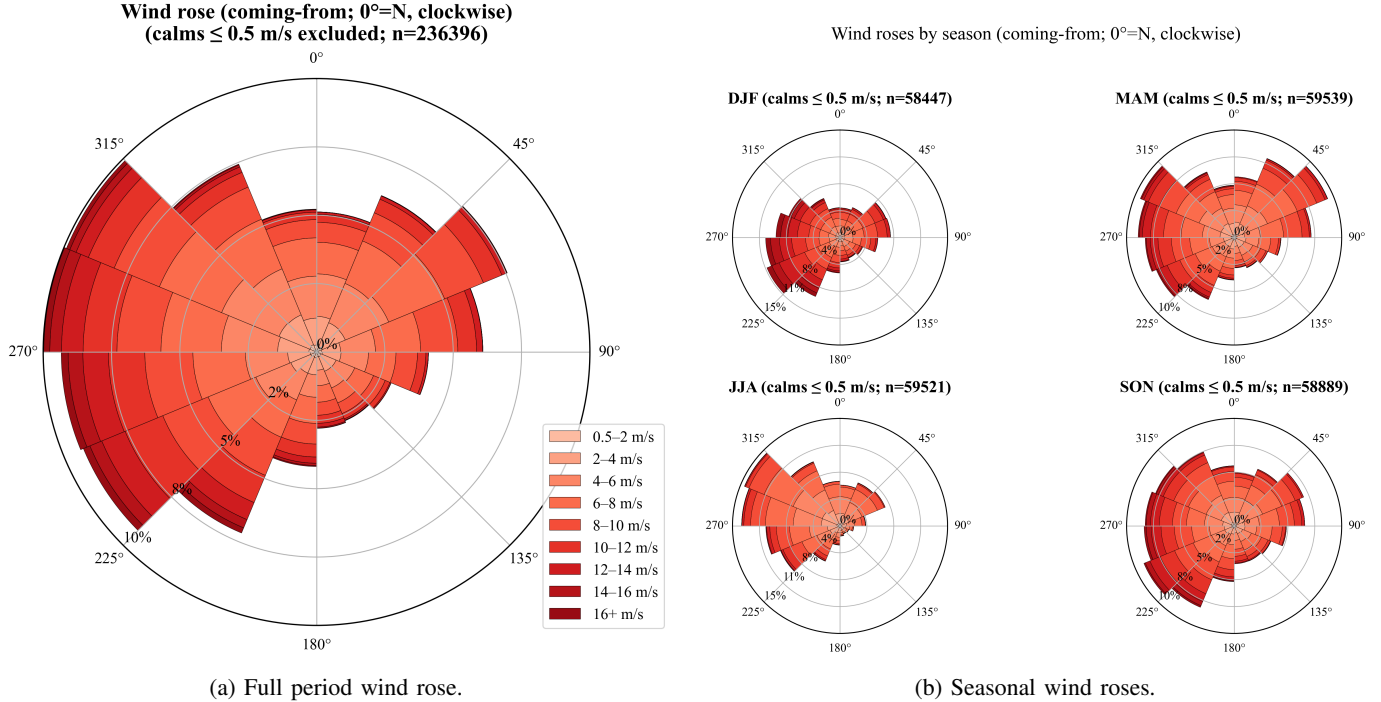


Figure 7: Prevailing W–WNW winds with winter intensification. Polar occurrence roses of hourly wind over 1994–2020 constructed with the coming-from convention ($0^\circ = N$, clockwise). Calms ≤ 0.5 m/s excluded for rose construction only. Directional sectors 22.5° ; speed classes $[0.5, 2], [2, 4], \dots, \geq 16$ m/s.

The full-period wind rose shows a concentration in western quadrants, with most occurrences between 4 and 12 m/s and smaller contributions up to 14–16 m/s. The modal sectors lie between west and west-north-west. The seasonal roses show persistence

of the western approach in all seasons, with a clear winter increase in the occupancy of higher speed bins. A modest veer toward west-north-west appears in spring and summer, and speeds are lowest in summer.

A short physical interpretation is useful for context. The winter enhancement in both wind frequency and speed aligns with the mid-latitude North Atlantic storm track, which shifts equatorward and intensifies, yielding more frequent strong westerlies. During spring and summer the Azores High expands and shifts poleward, favouring slightly more north-westerly, weaker conditions. This synoptic modulation explains the observed seasonal veer and amplitude differences without invoking local effects.

The information sought from the current roses was the dominant flow axis and whether it varies with season. Occurrence roses under the going-to convention after 180° rotation of the reported headings for consistency with the hydrodynamic convention were computed, with calms excluded. The relevant results are presented in figure 8.

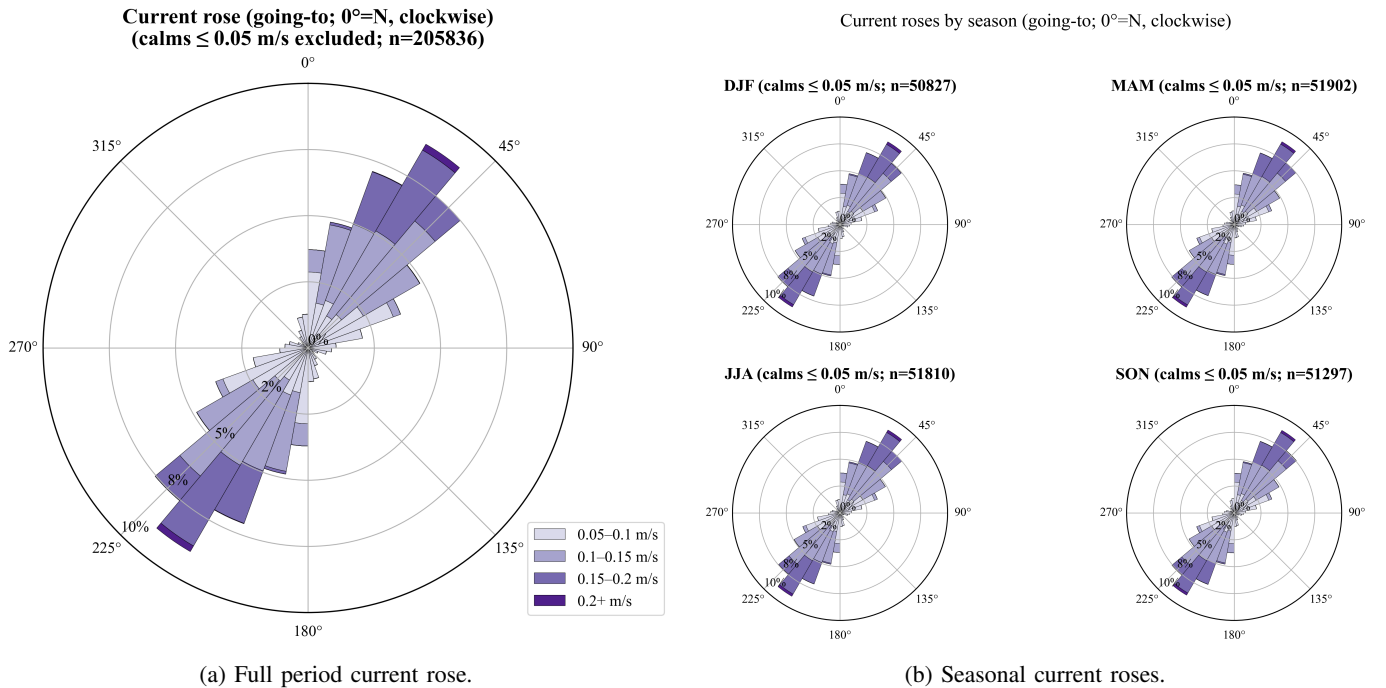


Figure 8: Tide-dominated NE–SW bidirectional current regime with weak speeds. Polar occurrence roses of hourly depth-averaged currents from RESOURCECODE over 1994–2020 constructed with the going-to convention ($0^\circ = N$, clockwise). Calms ≤ 0.05 m/s excluded for rose construction only. Directional sectors 10° ; speed classes [0.05, 0.10), [0.10, 0.15), [0.15, 0.20), ≥ 0.20 m/s.

The full-period current rose displays two narrow, opposing lobes aligned approximately along a NE–SW axis. Visual inspection of the modal sectors indicates peaks near $25^\circ \pm 5^\circ$ and $215^\circ \pm 5^\circ$ (going-to), consistent with a reversing tidal jet. Most currents fall below 0.20 m/s with frequent 0.10–0.20 m/s occurrences. The seasonal roses show that the NE–SW axis persists with little change in occupied speed classes across seasons. The bidirectional structure confirms a tide-dominated regime and explains why an overall mean current direction is not meaningful.

Arithmetic mean speeds and circular mean directions by season and overall were calculated, with wind as coming-from and currents as going-to. Hence, table III was produced to provide a compact summary of seasonal and overall averages for speeds and directions, consistent with the roses.

Table III: Seasonal and overall mean wind and current conditions, 1994–2020. Wind directions are coming-from and computed as circular means; wind speeds are arithmetic means. Current directions are going-to; the overall mean current direction is omitted because reversing tidal flow renders a single bearing uninformative.

Group	Wind speed [m/s]	Wind dir [$^\circ$]	Current speed [m/s]
Overall	7.22	296.6	0.10
DJF	8.67	266.3	0.10
MAM	6.95	321.1	0.10
JJA	6.00	302.6	0.10
SON	7.31	287.5	0.10

Two practical caveats follow. First, the RESOURCECODE current field is barotropic and tidally forced, *i.e.*, depth-averaged and without stratification, so residual wind-driven or baroclinic signals are not fully represented; the roses and means should therefore be interpreted as tidal-dominant descriptors rather than complete current climatology. Second, because reversing tidal flows collapse circular averages, reporting a single current bearing would be misleading; the bidirectional axis and modal headings are the informative quantities for design and operations.

In conclusion, the site exhibits a prevailing W–WNW wind regime with stronger conditions in winter and weaker conditions in summer, while the current field is tide-dominated with a stable NE–SW axis centred near $25^\circ/215^\circ$ and weak magnitudes. These integrated results are consistent with a monthly climatology and are sufficient for the present purpose of characterising mean metocean forcing.

E. Comparison to wave buoy measurements

The purpose of this subsection is to evaluate how faithfully the RESOURCECODE hindcast reproduces observed sea states near the study site and to quantify the resulting uncertainty. The focus is on the root-mean-square differences (RMSD) between hindcast and observations for significant wave height H_s , mean period T_{m02} , and mean direction, followed by an assessment of representativeness limits arising from depth and position mismatch.

1) Methodology: Validation uses Candhis buoy 05602 (Belle-Île) at $(47.2850^\circ, -3.2850^\circ)$ where the water depth is $h \approx 45$ m, and the RESOURCECODE node at $(47.3236^\circ, -3.5522^\circ)$ located in $h = 93.32$ m [2], [1]. The two points are separated by about 21 km, with the RESOURCECODE node lying farther offshore and in deeper water.

Paired samples are formed by matching each buoy timestamp to the closest hindcast value within a ± 30 min tolerance in UTC. This ensures like-for-like meteorological forcing while retaining a sufficient number of pairs over the 2020 overlap.

QC removes sentinels and non-physical values and rejects spectra that fail simple shape checks, here $|\text{SKEW}| \leq 0.3$ and $\text{KURT} \leq 5$. When available, non-valid QUALITE labels are excluded. These steps avoid inflating errors with data that are known to be unreliable.

Directional consistency is enforced by expressing both series as coming-from. If a source is reported as going-to, it is rotated by 180° . Because direction is circular, differences are computed as minimal wrapped angles in $[-180^\circ, 180^\circ]$ before summarising.

Error metrics are computed as the RMSD for H_s and T_{m02} and as the circular RMSD for direction based on the wrapped differences. These metrics provide scale-aware summaries that weight all paired events equally across the year.

2) Results and Interpretations: Table IV shows a compact quantification of the model–observation discrepancies and the effective sample size after QC and time pairing. RMSD for H_s and T_{m02} and circular RMSD for direction using the paired 2020 half-hours were calculated.

Table IV: Hindcast reproduces Belle-Île buoy sea states in 2020 with small height and period errors and moderate directional spread. Pairs were formed by matching Candhis 05602 at $(47.2850^\circ, -3.2850^\circ)$, $h \approx 45$ m, to RESOURCECODE node 117231 at $(47.3236^\circ, -3.5522^\circ)$, $h = 93.32$ m, within ± 30 min (UTC). QC retained only valid records (sentinels and non-physical values removed; spectra with $|\text{SKEW}| \leq 0.3$ and $\text{KURT} \leq 5$; non-valid QUALITE excluded when available) [2].

Metric	RMSD	Pairs used
H_s (m)	0.39	15 947
T_{m02} (s)	0.84	15 947
Direction (deg)	21.2	15 947

In the table, height and period errors are small relative to the full range of observed conditions, while the directional circular RMSD is moderate. The large sample size indicates that the pairing and filters retain most of the year, which stabilises the summary statistics.

It is observed that the hindcast captures the first-order variability in both energy and timescale, with residual differences that merit inspection at event level and across the distribution. The table motivates a complementary analysis in time and value space to diagnose when and how the discrepancies arise.

Figure 9 was produced to show whether the hindcast follows the observed temporal evolution of storms and calms, and how directional differences behave through time. The figure overlays the paired time series of H_s and T_{m02} and plots the wrapped directional error for each pair to expose timing drifts and episodic departures that a single scalar metric may hide.

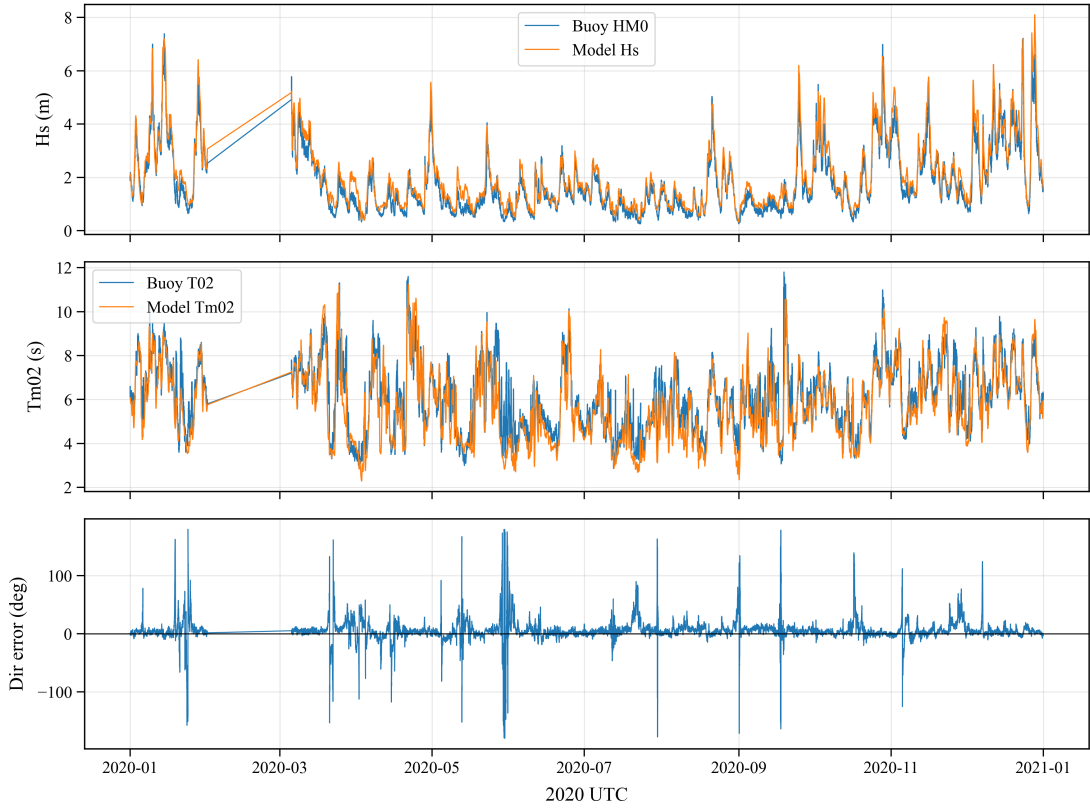


Figure 9: Hindcast time series track observed storm build-up and decay; directional differences remain near zero except for brief spikes. Paired 2020 values were formed with ± 30 min matching; mean directions use the coming-from convention, and the plotted angular error is (model–buoy) wrapped to $[-180^\circ, 180^\circ]$. Sample size $N = 15,947$; gaps indicate missing or rejected observations.

In the figure, the hindcast tracks the build-up and decay of winter storms and the quieter summer background, with small deviations that increase during the most energetic events. Directional errors cluster near 0° for long periods, but show intermittent spikes that coincide with rapidly evolving weather or weak-sea states.

The amplitude and timing are reproduced at synoptic scale, while the largest seas amplify small phase or spectral-shape discrepancies and the most variable directional regimes generate short-lived angular departures. Such behaviour is expected when comparing an offshore, grid-averaged hindcast with a point measurement closer to the coast.

The information sought with figure 10 was whether discrepancies depend on magnitude and whether systematic tilt or non-linearity is present. The experiment plots model–observation scatter for H_s and T_{m02} against the 1:1 line and the histogram of wrapped directional errors; panel titles report the corresponding RMSD to link the graphics to table IV.

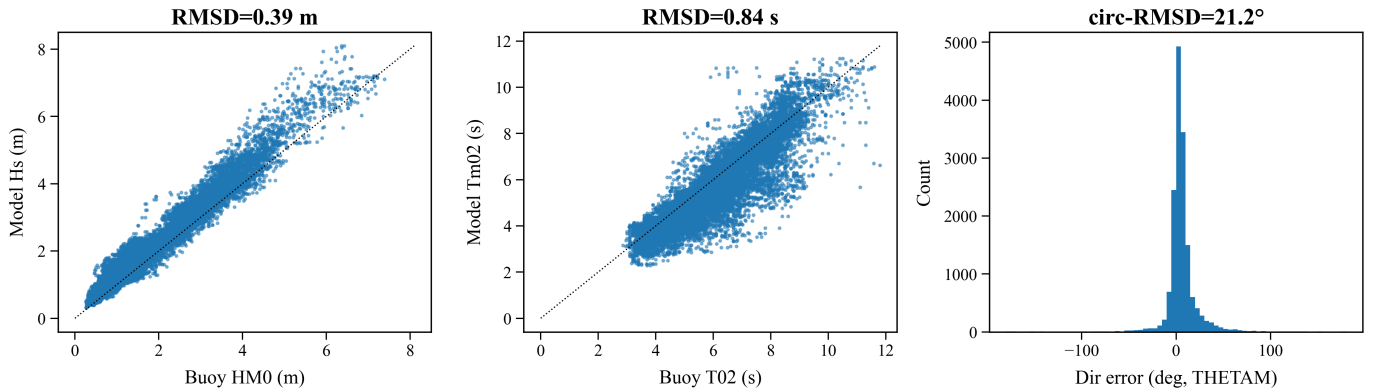


Figure 10: Agreement is close to the 1:1 line for H_s and T_{m02} with mild fan-out at the largest seas; directional errors are centred near 0° with thin tails. Paired 2020 values after QC were used; scatter panels compare model to buoy against the 1:1 line, and the histogram shows the wrapped angular error (model–buoy). Sample size $N = 15,947$.

In the figure, H_s lies close to the 1:1 line up to ~ 8 m with a slight fan-out at the highest values, whereas T_{m02} exhibits broader dispersion at long periods without a strong slope bias. Direction errors form a compact peak around 0° with thin tails and a few outliers.

The interpretation is consistent with table IV: height skill is good with modest spread during storms, the longest-period swell is harder to match due to small spectral-shape differences, and a circular RMSD near 21° is plausible in a coastal setting where mixed sea–swell and refraction produce fast directional changes. Bias and scatter index could complement RMSD in future work to separate systematic offset from random spread, but they are not required for the present objective.

Representativeness effects arising from depth and position are material to the comparison. Using the deep-water threshold $h/L_0 > 0.5$ with $L_0 = gT^2/(2\pi)$ gives $T_{\text{deep}} \approx \sqrt{4\pi h/g}$, yielding $T_{\text{deep}} \approx 7.6$ s at $h \approx 45$ m (buoy) and $T_{\text{deep}} \approx 10.9$ s at $h = 93.32$ m (hindcast node). A larger fraction of the buoy’s energy thus propagates in transitional depth, where refraction, shoaling, and partial sheltering by Belle-Île can rotate and redistribute energy before measurement, while the offshore hindcast remains in deep water for more cases.

The horizontal offset of about 21 km further exposes the comparison to along-coast gradients during storms and to mesoscale variability not resolved by a single point-to-point pairing. These mechanisms explain much of the residual error structure, in particular the episodic direction spikes and the increased spread for long-period swell.

A data-gap is present in late winter and early spring. The missing segment arises from the observations rather than the model and results from the combination of telemetry outages and the application of the QC thresholds. The plotted series bridge over those periods, and no paired points are counted there.

In conclusion, the 2020 Candhis–RESOURCECODE comparison yields RMSD of 0.39 m for H_s , 0.84 s for T_{m02} , and 21.2° for direction across 15,947 paired half-hours. Given the depth and position mismatch, the agreement is adequate for site characterisation and for contextualising the extremes analysis that follows.

IV. EXTREME WAVE CONDITIONS

A. Extreme Value Analysis (EVA)

Design of offshore wind turbines requires estimates of rare sea states in order to verify ultimate limit states. EVA provides a statistical framework to extrapolate significant wave height H_s beyond the historical record and to express design conditions as return values associated with specified return periods, *e.g.*, 1 and 50 years.

The analysis uses the 1994–2020 hourly hindcast at the Bretagne Sud site from the RESOURCECODE database and adopts a working assumption of statistical stationarity over the record. Basic screening for completeness and physical plausibility was applied so that inferences reflect environmental variability rather than data artefacts.

Two complementary univariate approaches are employed to characterise the upper tail of H_s . The block–maxima (BM) method extracts one maximum per year and fits a Generalised Extreme Value (GEV) distribution. The peaks–over–threshold (POT) method selects storm peaks over a high threshold and fits a Generalised Pareto Distribution (GPD). The pair provides cross–checks because BM emphasises the most severe event in each year, whereas POT uses many more independent extremes [6].

Outputs reported in the following subsections are the 1-year and 50-year return values of H_s with confidence intervals, together with characteristic peak periods T_p and mean approach directions associated with the extreme events for use in design load cases. A brief comparison to a multivariate environmental contour is included to place the univariate results in joint (H_s, T_p) space.

B. Block maxima (BM) method

The aim was to estimate design return levels for significant wave height H_s under a stationary climate. The target quantities were the T -year return levels z_T between $T = 1.01$ and 50 years together with uncertainty.

1) Methodology: The hourly H_s record from 1994 to 2020 was partitioned into non-overlapping annual blocks of 365.2425 d, and the maximum in each block was extracted, yielding $n = 27$ annual maxima. Independence was enforced by construction at the block scale, and a stationary GEV distribution was fitted to these maxima by maximum likelihood.

Model adequacy was assessed with a return-value overlay, a probability-density comparison, and quantile–quantile (Q–Q) and probability–probability (P–P) plots. Empirical plotting positions used $(n + 1)/\text{rank}$ on a logarithmic return-period axis. Pointwise 95 % confidence intervals for return levels were obtained from the fitted model.

2) Results and interpretations: The temporal distribution of annual maxima was inspected to verify coverage and to characterise seasonality. Figure 11 shows the time series with the annual maxima highlighted.

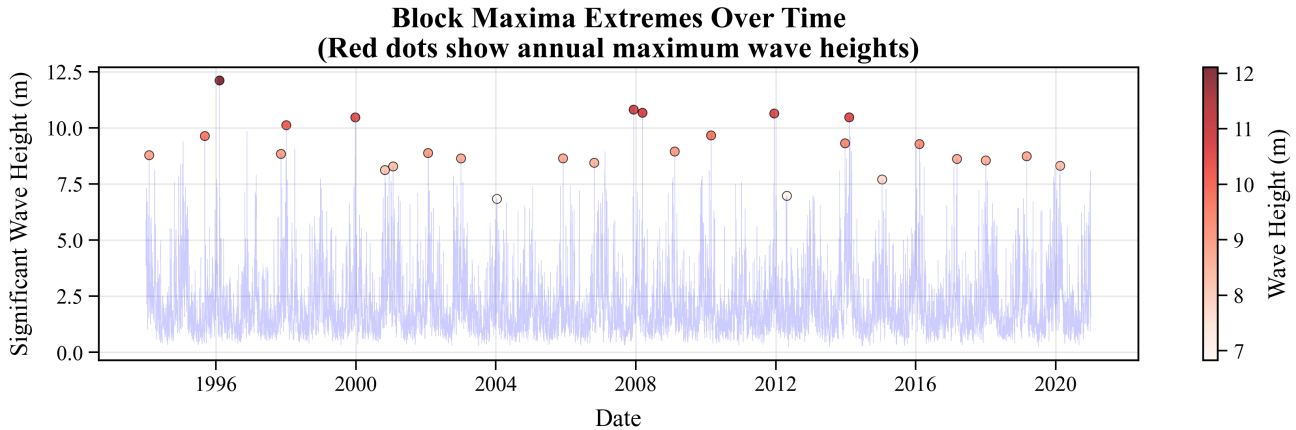


Figure 11: Annual storm peaks are winter-dominated, without secular trend (1994–2020). Hourly significant wave height H_s was partitioned into non-overlapping 365.2425 d blocks, and the maximum from each block ($n = 27$) was extracted and overlaid on the parent series; colour maps H_s .

Annual peaks occur throughout the record with values spanning about 7–12 m, and larger events are winter-dominated. No persistent widening or upward drift of the envelope is apparent.

It is interpreted that interannual variability is substantial but not directional in time, which supports the stationarity assumption used for the GEV fit and indicates that a representative peak was captured each year.

Model adequacy was then evaluated to ensure reliable extrapolation to engineering horizons. The information sought was whether the fitted GEV replicates sample quantiles and densities, including the upper tail. Hence, empirical and model quantiles and densities were compared using the standard diagnostic suite in figure 12.

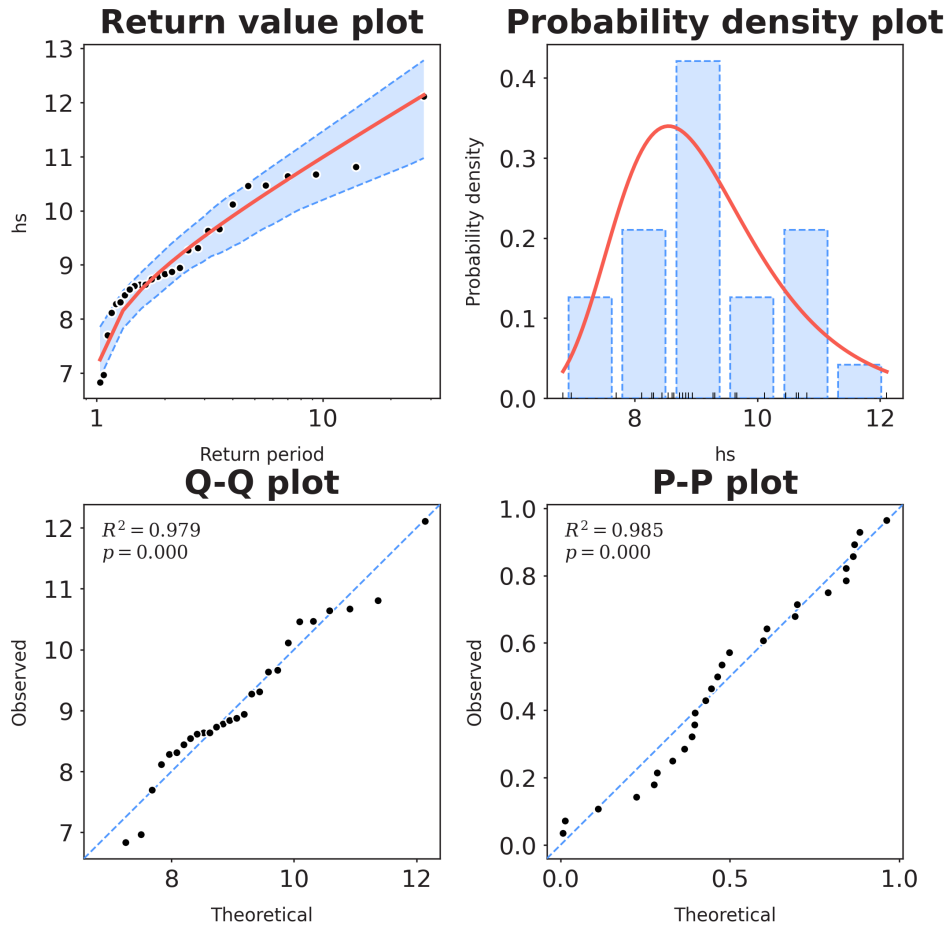


Figure 12: Stationary GEV adequately represents the annual maxima. A GEV model was fitted by maximum likelihood to $n = 27$ BM (1994–2020). Diagnostics comprise a return-value overlay (with 95% CI) and histogram–density comparison, and Q–Q/P–P plots.

Empirical and model quantiles align closely along the one-to-one lines, with only minor curvature at certain points where sampling is sparse. The model density follows the histogram over the observed range.

It is concluded that a stationary GEV provides an adequate summary of the annual maxima and is suitable for extrapolation to multi-decadal return periods, with uncertainty driven by the limited $n = 27$.

Return levels were then quantified and compared with empirical plotting positions. The information sought was z_T and their 95 % confidence intervals, together with a visual check of consistency. The fitted curve and confidence band against empirical points were plotted as shown in figure 13.

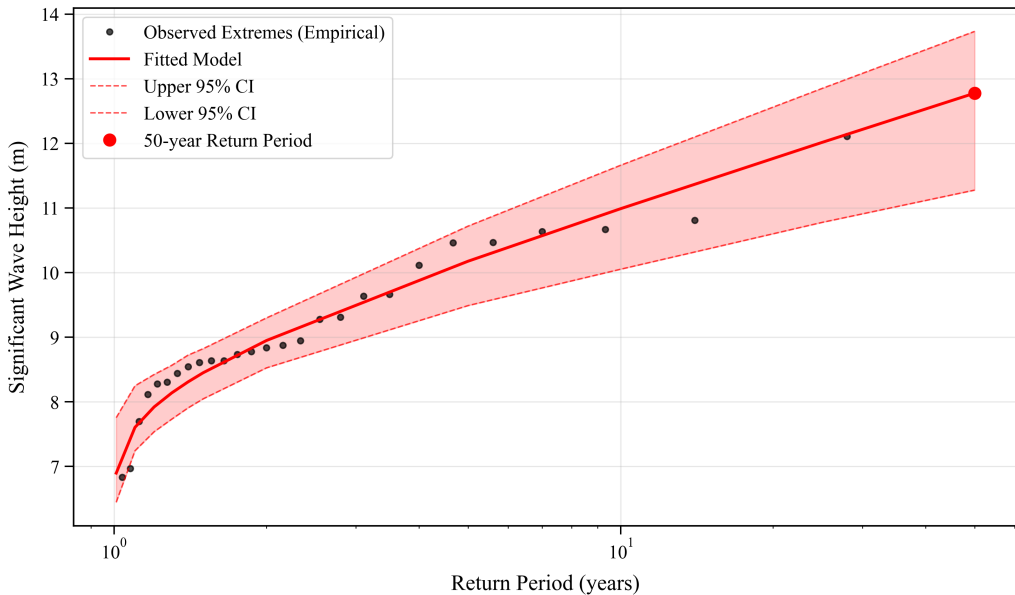


Figure 13: The return-level curve from the BM-GEV fit gives $z_{50} = 12.78$ m with moderate uncertainty. Empirical plotting positions for the $n = 27$ annual maxima use $(n + 1)/\text{rank}$ on a logarithmic return-period axis. The fitted stationary GEV and its pointwise 95 % confidence band are shown. Empirical points track the model up to ~ 25 years, and uncertainty widens toward 50 years where observations are absent.

Empirical points lie near the fitted curve across $T \in [1, 25]$ years, and the band widens moderately toward 50 years where no data exist. The highlighted 50-year estimate lies within the model envelope.

Numerical estimates for several return periods T are reported in table V.

Table V: Design return levels for significant wave height obtained from a stationary GEV fitted to $n = 27$ annual maxima (1994–2020). Reported are point estimates z_T and pointwise 95 % confidence intervals for $T = \{1.01, 2, 5, 10, 50\}$ years.

Return period T (years)	Return level z_T (m)	95 % CI (m)
1.01	6.90	[6.47, 7.84]
2	8.95	[8.52, 9.43]
5	10.18	[9.62, 10.67]
10	10.99	[10.17, 11.64]
50	12.78	[11.34, 13.83]

The observations indicate $z_{1.01} \approx 6.90$ m and $z_{50} \approx 12.78$ m, with the latter bounded by [11.34, 13.83] m. The winter dominance and absence of temporal drift support the stationary fit over 1994–2020, and the resulting T -year levels are suitable for preliminary design checks before comparison with POT and joint (H_s, T_p) contours.

C. Peaks Over Threshold (POT) Method

The aim was to estimate design return levels of significant wave height H_s from the upper tail of the hourly hindcast and to verify that the fitted tail model is adequate for extrapolation to engineering return periods.

1) Methodology: The POT threshold was set at the 99th percentile of hourly H_s over 1994–2020 after testing multiple threshold-setting approaches; this choice balances sample size and extremeness by yielding enough independent exceedances while limiting contamination from non-extreme sea states. The selected value was $\hat{u} \approx 6.46$ m.

Independence was promoted with a declustering window of 48 h that retained only the highest peak within any 48 h period above the threshold. The excesses ($H_s - \hat{u} \mid H_s > \hat{u}$) were then modelled with a stationary GPD. Return levels z_T were derived for annual return periods with a civil year of 365.2425 d and pointwise 95 % confidence intervals were obtained from the model summary. Standard diagnostic plots were generated to check fit quality.

2) *Results and Interpretations:* The information sought with the diagnostic figure was whether the stationary GPD provides an unbiased description of the sampled tail. Therefore, a comparison was made between empirical exceedances and model predictions in probability, quantile, and density spaces using Q-Q and P-P plots and an overlaid density. The results are presented in figure 14.

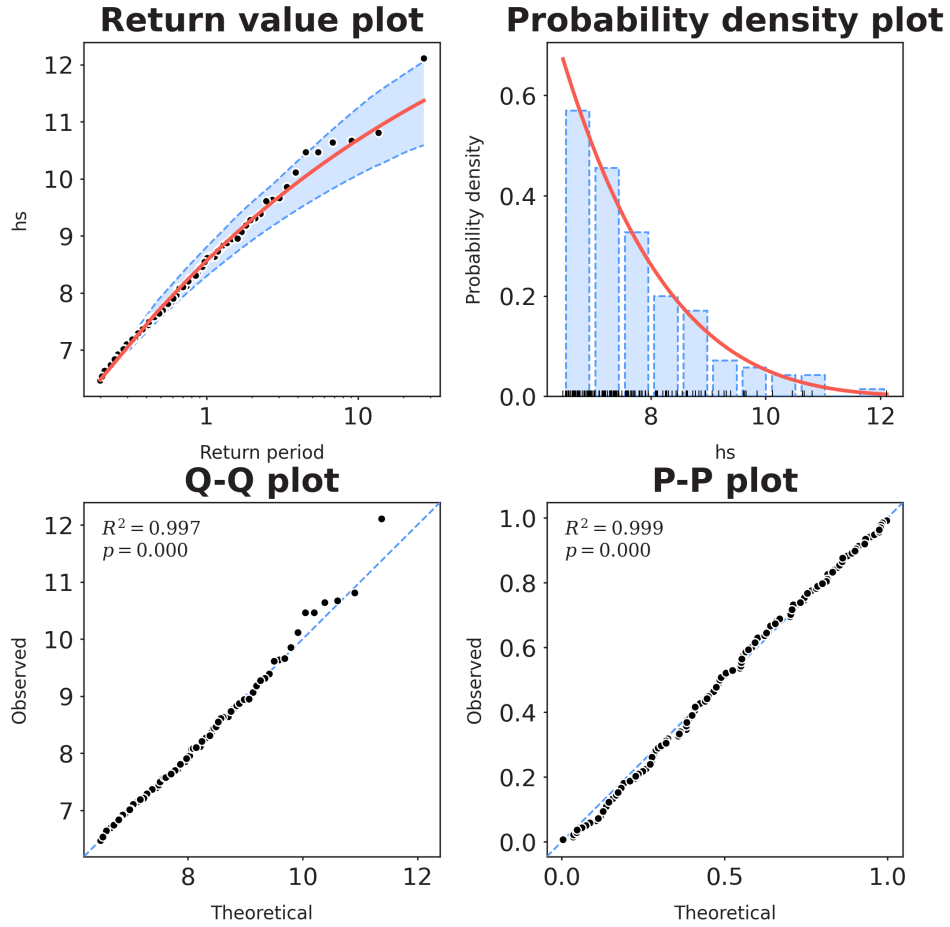


Figure 14: Diagnostics support an adequate GPD tail for declustered H_s exceedances. Hourly hindcast data for 1994–2020 were screened using a POT approach with the threshold fixed at the 99th percentile ($\hat{u} \approx 6.46$ m) and a 48 h runs rule to retain independent peaks. A stationary GPD was fitted. Shaded regions denote pointwise 95 % model bands that envelope the empirical behaviour over the sampled support.

The points track the reference lines closely and the model density follows the empirical histogram over the observed support. This pattern indicates that the fitted GPD captures the distribution of declustered exceedances without systematic bias and can be used to compute return levels.

Figure 15 was produced to obtain the set of design H_s levels across target return periods together with their uncertainty. This consisted in mapping empirical plotting positions and the fitted GPD curve onto the return-period axis and visualising pointwise confidence bands.

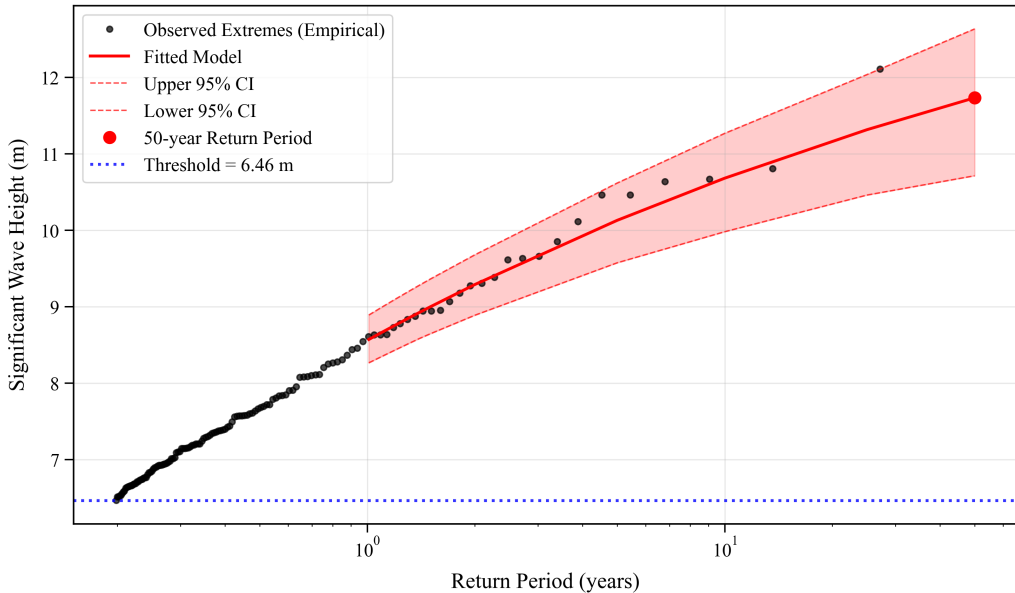


Figure 15: POT return-value curve indicates $z_{50} = 11.73 \text{ m}$ (95 % CI [10.71, 12.63]) and $z_{1.01} = 8.57 \text{ m}$ (95 % CI [8.27, 8.89]) for significant wave height. Exceedances of the 99th-percentile threshold ($\hat{u} \approx 6.46 \text{ m}$) were declustered with a 48 h window and fitted with a stationary GPD.

Empirical points lie near the fitted curve and within the uncertainty band in the data-rich region, while the band widens progressively with T , which reflects increasing extrapolation uncertainty as governed by the estimated tail shape.

Reading from the fitted summary gives $z_{1.01y} = 8.57 \text{ m}$ with a 95 % interval [8.27, 8.89] m and $z_{50y} = 11.73 \text{ m}$ with 95 % interval [10.71, 12.63] m. The short-horizon level is constrained by many exceedances near \hat{u} , whereas the 50-year level carries wider uncertainty due to sensitivity to the tail parameter.

Table VI compiles design values for the required return periods. Estimates are pointwise return levels from the stationary GPD with 95 % confidence intervals.

Table VI: Design return levels for H_s from a stationary GPD fitted to a declustered POT sample of the 1994–2020 hourly hindcast. The threshold was the 99th percentile ($\hat{u} \approx 6.46 \text{ m}$) and a 48 h runs rule enforced independence. Uncertainty increases with T as extrapolation grows.

Return period T (years)	Return level z_T (m)	95 % CI (m)
1.01	8.57	[8.27, 8.89]
2	9.29	[8.89, 9.68]
5	10.13	[9.58, 10.62]
10	10.68	[9.98, 11.27]
50	11.73	[10.71, 12.63]

The agreement between empirical plotting positions and the fitted curve in figure 15, together with the near-linear behaviour of the Q-Q and P-P plots in figure 14, supports the adequacy of a stationary GPD for this site. The widening intervals with T quantify the epistemic growth away from the threshold and should be propagated to design load cases and compared directly with the BM results in the subsequent subsection.

D. Comparison of BM vs POT Results

The purpose of this subsection is to assess how the BM and POT methods characterise extreme sea states at the study site and to determine whether they produce consistent design conditions. The comparison proceeds in two steps. First, the return value estimates of significant wave height H_s are compared at engineeringly relevant return periods. Second, the physical characteristics of the extreme events extracted by each method are examined to identify whether the two samples describe the same physical phenomenon. The subsection closes with an interpretation of which method is more appropriate for design and how the two methods should be used together.

1) Comparison of Return Value Estimates: The information sought in this subsection is whether the BM and POT methods provide statistically compatible return values for H_s at short and long return periods that are relevant for operability and ultimate limit state design, *i.e.*, $T = 1$ year and $T = 50$ years.

To obtain this information, the fitted extreme value models described earlier were sampled at $T = 1$ year and $T = 50$ years. The BM method produced $n = 27$ annual maxima over 1994–2020, whereas the POT method yielded $n = 137$ independent extreme events. The “1-year” level corresponds to the modelled 1.01 year return period, which is numerically indistinguishable at the reported precision and is treated here as the 1-year level. In both cases, 95% confidence intervals were obtained from the fitted models. For context, simple differences $\Delta = \text{BM} - \text{POT}$ are reported.

The resulting comparison is presented in table VII, which summarises the H_s return levels for the BM and POT fits at 1 year and 50 years, together with their uncertainty ranges and the direct difference between the two estimates.

Table VII: Comparison of BM and POT return levels for significant wave height H_s at selected return periods. Values are given in metres with 95% confidence intervals (CI). Δ is defined as BM–POT. BM uses annual maxima fitted with a GEV distribution ($n = 27$). POT uses a 99th percentile threshold with 48 h declustering fitted with a GPD ($n = 137$).

Return period	BM H_s (m) [CI]	POT H_s (m) [CI]	Δ (m)
1 year	6.90 [6.45, 7.76]	8.57 [8.27, 8.89]	-1.68
50 years	12.78 [11.28, 13.73]	11.73 [10.71, 12.63]	+1.04

Table VII shows two distinct regimes. At the 1-year horizon, the POT method predicts a higher H_s than the BM method. The BM 1-year level is 6.90 m with a 95% confidence interval of [6.45, 7.76] m, whereas the POT 1-year level is 8.57 m with [8.27, 8.89] m. The difference Δ is -1.68 m, which indicates that BM underestimates the short-return-period level relative to POT by more than 1.6 m.

This behaviour is consistent with the sampling strategy: the BM method retains only one value per year, which discards sub-annual storms, whereas the POT method retains all sufficiently large storms, subject to the declustering rule. Near the threshold, the GPD fit is therefore better constrained than the GEV fit, which reduces small-sample bias and produces higher short-period levels.

At the 50-year horizon, the ordering reverses. The BM method gives 12.78 m [11.28, 13.73] m, whereas the POT method gives 11.73 m [10.71, 12.63] m. The difference Δ is now +1.04 m, so BM exceeds POT by about 1 m at design scale. The two 95% confidence intervals overlap at 50 years, which indicates that the BM and POT estimates are statistically compatible at this horizon.

The widening of the confidence intervals at long return periods reflects the fact that both models are extrapolating well beyond the observed record length, which is only 27 years. The practical implication is that, for ultimate limit state design at $T = 50$ years, the two methods are consistent within uncertainty.

The combined result of table VII is that the BM and POT return-level curves cross at an intermediate return period. At short return periods, the POT method is more conservative, whereas at long return periods the BM method becomes more conservative. This crossing is typical of situations in which the BM fit assigns more weight to a few exceptional storms, which steepens the tail, whereas the POT fit smooths the tail based on a larger number of moderately extreme events.

For engineering use, this means that the POT method should be preferred when assessing frequent operating extremes such as a 1-year sea state, because it exploits more data near the threshold, while the BM method provides a useful upper envelope at rare design horizons where only the most severe historical storms are relevant.

2) Associated Wave Period, Direction, and Seasonality: The purpose of this subsubsection is to determine whether the BM and POT extractions describe the same physical storm environment by comparing the associated peak wave period T_p , approach direction, and timing of the extracted extremes. Establishing physical consistency between the two samples is necessary for a meaningful comparison of their return-level estimates.

Sea-state attributes were isolated concurrent with each extracted extreme. For BM, the timestamps of the 27 annual maxima were used to sample T_p and coming-from direction from the parent hindcast; for POT, the same attributes were sampled at the 137 exceedances above the 99th percentile after 48 h declustering. For each sample, empirical T_p quantiles (10 %, 50 %, 90 %) were computed, and circular means and circular standard deviations were calculated for directions using the coming-from convention, clockwise from true North. A seasonal count was compiled for the BM maxima.

To visualise how the periods of POT extremes sit within the parent distribution, the quantiles of T_p for POT events were overlaid on the histogram of all T_p values. The resulting graphic is provided in figure 16.

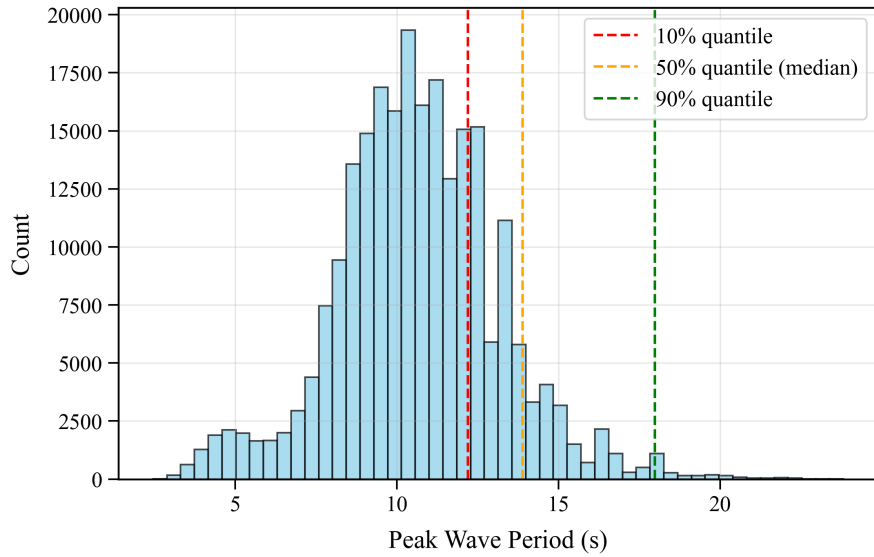


Figure 16: POT extremes occupy the mid-teens of the parent T_p distribution. Methods: POT exceedances above the 99th percentile with 48 h declustering ($n = 137$); dashed lines mark the 10 %, 50 %, and 90 % quantiles of T_p for the POT sample. Quantiles: 12.20 s, 13.89 s, and 17.99 s, respectively.

Figure 16 shows that POT extremes concentrate in the mid-teens with a relatively narrow interquartile range. The POT median aligns with the shoulder of the parent distribution, while the 90 % quantile lies well into the long-period tail, which is consistent with energetic winter storm seas, *i.e.*, fetch-limited wind-sea growth transitioning toward swell.

A similar plot was made for the BM maxima to examine whether the single largest storm in each year exhibits systematically longer peak periods. The quantiles of T_p for BM events were overlaid on the same parent histogram; the result is provided in figure 17.

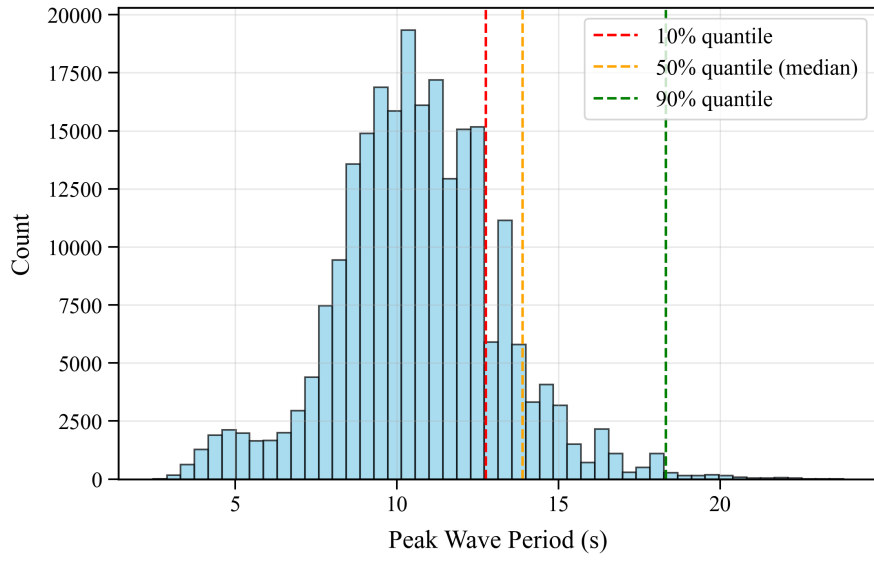


Figure 17: BM maxima exhibit similar T_p to POT extremes with a slightly longer upper tail. Methods: 27 annual maxima ($n = 27$); dashed lines mark the 10 %, 50 %, and 90 % quantiles of T_p for the BM sample. Quantiles: 12.76 s, 13.89 s, and 18.32 s, respectively.

Figure 17 indicates that the BM sample shares the same median T_p as POT but has a marginally longer 90 % quantile, which reflects the emphasis of BM on the most energetic yearly storms and supports a slightly longer upper-tail period content.

The quantitative summary of periods, directions, and timing is presented in table VIII. The table reports T_p quantiles for both extreme-event sets, circular directional statistics for both sets and the full record, and the seasonal distribution of BM

maxima.

Table VIII: Physical characteristics of extracted extreme events. BM uses annual maxima ($n = 27$). POT uses exceedances of the 99th percentile of H_s with 48 h declustering ($n = 137$). Directions are coming-from, clockwise from true North.

Metric	BM	POT	Full record
Count	27	137	236,688
T_p 10 % quantile (s)	12.76	12.20	–
T_p 50 % quantile (s)	13.89	13.89	–
T_p 90 % quantile (s)	18.32	17.99	–
Mean direction (°)	255.94	260.42	275.49
Circular std (°)	11.64	12.58	34.48
Winter share (%)	77.8	–	–
Spring share (%)	7.4	–	–
Summer share (%)	0.0	–	–
Autumn share (%)	14.8	–	–

The table shows that both BM and POT extremes are associated with long-period seas with T_p in the mid-teens. The shared median of 13.89 s and closely matching 10–90 % ranges indicate that the additional POT events sample the same dynamical regime as the BM maxima, rather than a different class of storms.

Table VIII also shows pronounced directional focusing of extremes. BM maxima arrive from 255.94° with a circular spread of 11.64°, and POT exceedances from 260.42° with a spread of 12.58°, both within a west–south-west sector. The full record has a broader mean near 275.49° and a spread of 34.48°, which confirms that the largest H_s events arise from a preferred approach direction narrower than the climatological distribution.

The seasonal counts in table VIII indicate that 77.8 % of BM maxima occur in winter and none in summer, with the remainder in autumn and spring. This timing is consistent with the identified west–south-west approach sector and with the regional extra-tropical storm track that dominates in boreal winter.

In conclusion, the BM and POT samples are physically consistent: both capture winter storm seas approaching from west–south-west with tightly clustered directions and peak periods concentrated in the mid-teens. The BM sample accentuates the longest-period tail by construction, whereas the POT sample provides denser coverage of the same storm regime, which explains the small differences observed in return-level extrapolations without implying different generation mechanisms.

3) *Interpretations:* The results above indicate that BM and POT behave differently because they encode two different philosophies of extremeness. The BM method focuses on the single largest storm of each year and therefore gives disproportionate weight to a few exceptional historical events. This emphasis tends to steepen the extrapolated tail of the fitted GEV distribution, which explains why the BM curve in table VII eventually overtakes the POT curve and predicts a higher 50-year H_s .

The POT method, by contrast, treats extremeness as exceedance of a high threshold and preserves all distinct storms above that level. This produces a larger but still homogeneous sample, which constrains the distribution of typical severe storms and yields a higher 1-year H_s but a slightly flatter tail at long return periods.

From a design standpoint, these behaviours are complementary rather than contradictory. For frequent extremes such as the 1-year sea state, which constrain operating envelopes and survival of routine storms, the POT estimate is preferable because it is supported by many more observed events close to that return period and therefore exhibits narrower confidence intervals at $T \approx 1$ year.

For rare extremes such as the 50-year event, which inform ultimate limit state calculations, the BM result provides a useful check because it anchors the extrapolation on the most severe observed storms. The statistical compatibility of the two 50-year confidence intervals shows that both methods are consistent with the available data at design horizon and that neither method produces an outlying or implausible prediction.

The physical characterisation in table VIII shows that both BM and POT extremes correspond to the same storm archetype: long-period waves (T_p in the mid-teens), propagating from west–south-west within a narrow directional band of about ±12°, and occurring almost exclusively in winter.

This alignment indicates that the two statistical samples are not sampling different physical regimes but are instead two views of the same winter storm forcing. The differences in the fitted return levels in table VII therefore arise from sampling strategy and extrapolation behaviour, not from any shift in physical wave generation mechanisms.

In conclusion, the BM and POT methods are consistent with each other and with the physical understanding of the site. The POT method provides a stable characterisation of the frequent severe-sea-state envelope and should be used to define

short-return-period design and operability conditions. The BM method provides an upper-bound cross-check for rare design events and confirms that the POT-based extrapolation does not underestimate the 50-year H_s . Both methods point to the same environmental driver: energetic west-south-west winter storms with peak periods in the range 12–18 s. This convergence supports the use of these storms as the governing load cases for structural design at the study site.

E. Comparison to multivariate environmental contour

The purpose of this subsection is to assess whether a joint extreme model for significant wave height and wave period yields design conditions that are consistent with the univariate return levels, and to determine whether the joint model implies materially different admissible combinations of (H_{m0}, T) for a 50 year reliability target.

1) Methodology: The information sought was whether the 50 year joint envelope intersects the univariate 50 year heights at periods that characterise local storms, *i.e.*, around the median and decile periods of the extracted extreme events.

To obtain this information, a 50 year environmental contour was constructed using the modified I-FORM with a principal component analysis (PCA) dependence model [7]. Hourly hindcast sea states were expressed as pairs (H_{m0}, T) , with the sampling interval used as the sea-state duration to set the occurrence rate. The data were linearly transformed to uncorrelated principal components, the target reliability index was mapped to a closed curve in the standard normal space, and the curve was back-transformed to the physical (T, H_{m0}) plane to obtain the iso-exceedance set for a 50 year return period.

For comparability with the univariate EVA, the contour ordinate $H_{m0}(T)$ was read at periods representative of the storm sample derived previously. The representative periods were the median peak period near 14 s and the lower and upper deciles near 12 s and 18 s. The univariate 50 year heights were those obtained earlier from the BM and peaks-over-threshold (POT) methods, namely 12.8 m and 11.7 m, respectively.

2) Results and interpretations: Figure 18 compares the 50 year contour to the population of hindcast sea states and allows the contour ordinates to be read at storm-relevant periods. It shows the calculated 50 year environmental contour and the background cloud of hourly (T, H_{m0}) sea states used to fit the dependence model.

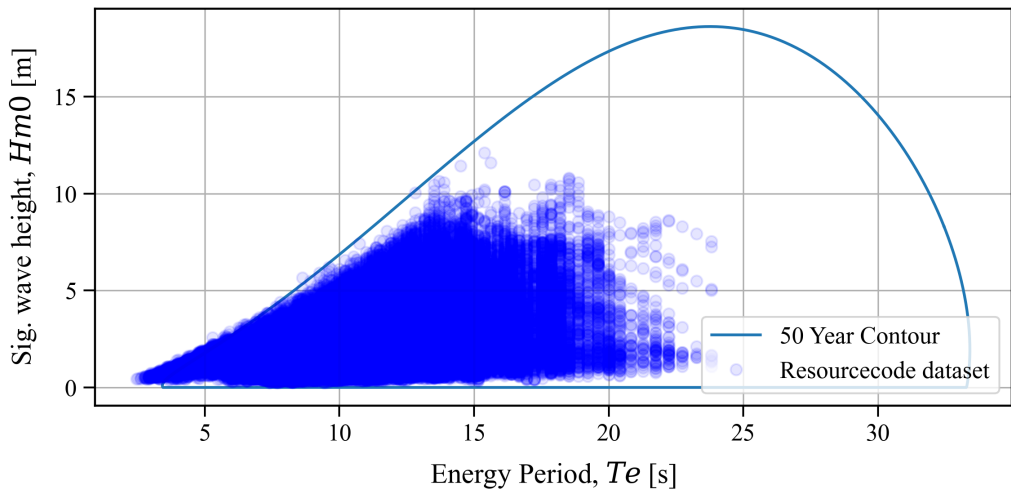


Figure 18: 50 year joint sea-state envelope for significant wave height H_{m0} and energy period T_e . The contour was computed with the PCA I-FORM method from hourly hindcast sea states over 1994–2020, using a 1 h sea-state duration; background points show the full (T_e, H_{m0}) sample.

The envelope lies above the observed cloud as expected for an iso-exceedance boundary. Reading the ordinate at $T \approx 14$ s gives $H_{m0} \approx 12.5\text{--}13.0$ m, decreasing to about 11–12 m at $T \approx 12$ s and increasing to about 15–16 m at $T \approx 18$ s. The contour exhibits a pronounced crest at very long periods, with a peak of approximately 18–19 m near $T \approx 23\text{--}24$ s, before descending toward longer periods.

These observations imply close agreement between the joint and univariate models within the storm-relevant period band. The BM 50 year height of 12.8 m coincides with the contour near the median storm period, while the POT value of 11.7 m lies inside the envelope across $T \approx 12\text{--}18$ s, indicating a conservative margin of roughly 0.5–1.5 m relative to the contour ordinate in this range. The substantially larger crest at very long periods reflects joint-tail extrapolation in the (H_{m0}, T) space rather than frequently sampled conditions and is therefore weakly constrained by the data at this site.

The multivariate contour and the univariate EVA address different statistical questions, which explains the divergence at very long periods. The univariate analyses estimate the marginal H_{m0} level exceeded, on average, once every 50 years, irrespective of the accompanying period. The environmental contour identifies the boundary of (H_{m0}, T) pairs whose joint exceedance probability corresponds to a 50 year return period, so its absolute maximum tends to occur at the tail of the period distribution where joint occurrence is rarer. This distinction accounts for the higher long-period crest while preserving consistency with univariate return levels over the period range that typifies local storms.

In conclusion, the 50 year contour corroborates the univariate design heights at realistic storm periods and supplies the admissible (H_{m0}, T) combinations required for structural load calculations. The long-period crest provides a useful sensitivity bound but should be treated cautiously for central design specification at this location.

V. CONCLUSION

The study characterised the mean and extreme wave climate at the Bretagne Sud 1 site using the 1994–2020 RESOURCECODE hindcast and translated the statistics into design inputs. Mean and seasonal behaviour were established, representativeness was checked against a nearby buoy, and rare events were quantified with complementary extreme value models.

Mean conditions were moderate and westerly: $\overline{H_s} = 2.09 \text{ m}$ and $\overline{T_{m02}} = 5.79 \text{ s}$ with a prevailing coming-from direction near 275.5° . A clear winter–summer cycle was present, yet no secular trends were detected over the 1994–2020 period in monthly means of height, period, or direction. More than 99.7% of hours satisfied deep-water criteria, which supports linear deep-water dispersion and kinematics for modelling.

Hindcast skill against Candhis buoy 05602 in 2020 showed RMSDs of 0.39 m for H_s , 0.84 s for T_{m02} , and 21.2° for direction. The error structure matched expectations from depth and location differences, indicating fitness for site characterisation and pre-design use.

Univariate extremes were consistent across methods. BM with GEV yielded H_s return levels of about 6.90 m at one year and 12.78 m at fifty years, while POT with GPD gave about 8.57 m and 11.73 m, with overlapping fifty-year intervals. Associated storms were winter-dominated, approached from west–south-west, and had T_p concentrated near 14 s within an interquartile span of 12 s to 18 s.

The multivariate fifty-year environmental contour in (H_{m0}, T) corroborated the univariate heights at storm-relevant periods, with ordinates near 12.5 m to 13.0 m at $T \approx 14 \text{ s}$. The long-period crest was interpreted as a joint-tail extrapolation useful for sensitivity analysis rather than a central design pairing.

Design application follows directly. Deep-water kinematics should be used, with directional checks centred on the west–south-west sector. For operability and frequent survival, the one-year POT level is appropriate; for ultimate limit state, H_s in the range 11.7 m to 12.8 m should be paired with T_p in the range 12 s to 18 s, and checked against the contour.

Further work should tighten uncertainty where it matters for loads, *i.e.*, non-stationary with covariates, directional spreading effects, nearshore transformation to turbine locations, and incorporation of additional observations for validation.

DECLARATION OF AI USE

ChatGPT (OpenAI) was used exclusively to refine the manuscript's language and formatting. All scientific interpretations, analyses, and conclusions remain the sole responsibility of the author.

ACKNOWLEDGEMENTS

I thank Luca Knab, who performed most of the . I also thank Prof. Marissa Yates for teaching the *Sea States, Wave Propagation, and Ocean Wave Energy* course and for bringing delicious baked treats to class. Code and notebooks were jointly maintained at https://github.com/Lucaschikashy/sea-states_project_bretagne.git. Hindcast wave data were provided by the RESOURCECODE consortium, and observational data from the Candhis Belle-Île buoy (05602) were consulted.



Figure 19: Photograph taken on 28/10/2025 at the southern coast of Bretagne, near the study site.

REFERENCES

- [1] M. Accensi, M. Alday, and C. Maisondieu, “RESOURCECODE: Wave hindcast database user manual,” Technical report Issue 1.3, Ifremer, Mar. 2022.
- [2] “Campagne 05602 belle-île.” https://candhis.cerema.fr/_public/_campagne.php?Y2FtcD0wNTYwMg==, 2025. CANDHIS, Cerema; accessed 2025-10-30.
- [3] “Bretagne sud 1.” <https://www.eoliennesenmer.fr/facades-maritimes-en-france/facade-nord-atlantique-manche-ouest/projet-en-bretagne-sud/bretagne-sud-1>, 2025. Éoliennes en mer en France; accessed 2025-10-30.
- [4] M. Cowles and C. Davis, “On the origins of the .05 level of statistical significance.,” *American Psychologist*, vol. 37, no. 5, p. 553, 1982.
- [5] M. L. Yates, “Linear wave theory,” Oct. 2025. Course lecture slides, MEC_5EO04_TA/MEC_53456_EP, Class 2, 3 October 2025.
- [6] M. L. Yates, “Extreme value analysis for waves: Class p3 presentation,” Oct. 2025. Course presentation slides for *Sea States, Wave Propagation, and Ocean Wave Energy*, École Polytechnique; 10 October 2025.
- [7] A. C. Eckert-Gallup, C. J. Sallaberry, A. R. Dallman, and V. S. Neary, “Application of principal component analysis (pca) and improved joint probability distributions to the inverse first-order reliability method (i-form) for predicting extreme sea states,” *Ocean Engineering*, vol. 112, pp. 307–319, 2016.